Particle-based model to simulate the micromechanics of biological cells

P. Van Liedekerke,* E. Tijskens, and H. Ramon
Department of BIOSYST, KULeuven, Leuven, Belgium

P. Ghysels, G. Samaey, and D. Roose
Department of Computer Science, KULeuven, Leuven, Belgium

(Received 16 December 2009; revised manuscript received 4 May 2010; published 3 June 2010)

This paper is concerned with addressing how biological cells react to mechanical impulse. We propose a particle based model to numerically study the mechanical response of these cells with subcellular detail. The model focuses on a plant cell in which two important features are present: (1) the cell's interior liquidlike phase inducing hydrodynamic phenomena, and (2) the cell wall, a viscoelastic solid membrane that encloses the protoplast. In this particle modeling framework, the cell fluid is modeled by a standard smoothed particle hydrodynamics (SPH) technique. For the viscoelastic solid phase (cell wall), a discrete element method (DEM) is proposed. The cell wall hydraulic conductivity (permeability) is built in through a constitutive relation in the SPH formulation. Simulations show that the SPH-DEM model is in reasonable agreement with compression experiments on an *in vitro* cell and with analytical models for the basic dynamical modes of a spherical liquid filled shell. We have performed simulations to explore more complex situations such as relaxation and impact, thereby considering two cell types: a stiff plant type and a soft animal-like type. Their particular behavior (force transmission) as a function of protoplasm and cell wall viscosity is discussed. We also show that the mechanics during and after cell failure can be modeled adequately. This methodology has large flexibility and opens possibilities to quantify problems dealing with the response of biological cells to mechanical impulses, e.g., impact, and the prediction of damage on a (sub)cellular scale.

DOI: 10.1103/PhysRevE.81.061906 PACS number(s): 87.17.Rt, 87.85.gp, 87.16.Gj

I. INTRODUCTION

Cellular systems—nature's building blocks—are one of the most studied systems because these microscopic units control the overall macroscopic behavior of animals and plants. With respect to their mechanics, plant cells are intuitively somewhat simpler than animal cells, since the former are mostly immobilized. Nevertheless, the physical nature of plant tissue remains challenging. It is intrinsically multiscale as it depends on the microstructure of the cells as well as on their structural arrangement (aggregate level). In addition, it is also a multiphysics problem, since apart from the immersed solid materials (e.g., cell wall, middle lamella), fluid and gas transport in the cells, through the cell walls and in the intercellular spaces, will play a role as well. In this respect the mechanics of plant tissue is considerably more complicated than other cellular materials such as metallic foams and trabecular bone, where a single material is the main load-bearing component.

Plant cells usually have a strong cell wall to protect them from hostile environments. Inside these cells, a quasi-incompressible liquid builds up a hydrostatic pressure (turgor pressure) through osmosis which is responsible for the cellular rigidity (wilting of low hydrated plants). The cellular mechanics in plants influences "slow" physiological processes inside the cell such as growth, development and most likely even gene expression [1–4]. It also plays a key role in short time scale processes such as bruise formation in fruit during impact and *rapid plant movement* in Venus Flytraps. Because of the difficulty to probe physical quantities at such scale experimentally, the microscopic subcellular mechanics that goes along with these processes remains for a great part uncomprehended and unquantified [5–7].

Therefore, in the past, relevant analytical models have been proposed to simulate the mechanics of cellular systems [8–14], yet with limited flexibility and applicability. Others have introduced finite element modeling (FEM), considering the elastic quasistatic response of a cell [15,16], or particle approaches, focusing more on the rheological properties [17]. Nevertheless, to get more insight in the micromechanical response of cellular systems, it remains essential to develop models which can capture and describe more subcellular detail, including differences in cell shapes and sizes, and the intercellular interactions [18,19].

This paper is concerned with building a model that can describe the mechanics of a cell in static and dynamic situations. To this end, we introduce a particle based method and focus on spherical shaped plant cells whereby a solid phase and a liquid phase are considered. Our approach is a combination of smoothed particle hydrodynamics (SPH) to model the liquid phase and a discrete element method (DEM) to describe the solid phase of the cell walls [6]. SPH is a mature mesh-free simulation method typically used in situations dealing with large deformations, discontinuities, and free boundaries. Originally developed in astronomical contexts [20], it has now become a versatile technique in modeling gas and fluid dynamics. The choice to apply SPH in biological systems lies also in the possibilities of modeling non-Newtonian liquids, viscoelastic liquids, water transport in porous media, multiphase flow, and diffusion (see, e.g.,

*Corresponding author. Present address: Department of BIOSYST, KULeuven, Kasteelpark Arenberg 30, Leuven, Belgium; paul.vanliedekerke@biw.kuleuven.be

[21–23]). Furthermore, mesh-free particle methods are quite suitable for coarse-graining and multiscaling approaches [24]. For example, the recent modeling technique smoothed dissipative particle dynamics (SDPD) couples the hydrodynamic interactions of SPH with thermal fluctuations in a thermodynamically consistent way [25–27]. Such formalism is useful in coarse-grained models of subcellular processes where these fluctuations become important.

The presented model here is primarily meant to predict force transmission and stresses in biological cells. We consider a parenchyma cell, which makes the bulk of plant tissue, and can be mechanically regarded as a stiff, thin walled vessel (the cell wall) containing a viscous fluid. The system as a whole is regarded as incompressible and isothermal. The focus is on short time scales, typically those arising at impact, where most long-term physiological responses are negligible. Due to the adaptivity and flexibility of the particle framework, this cell-centered approach can be extended adding other cells to form a multicellular system [6], supplying representative volume elements for computational homogenization to obtain tissue constitutive behavior [28,29]. On the other side, it can also be refined to capture the detail of the subcellular structure.

In the following, we give a detailed description of the model and compare it with the results of an analytical model and an experimental test case on an *in vitro* cell during quasistatic compression. Thereafter, we introduce two cell types: a *stiff* type, resembling a plant cell; and a *soft* type, which mimics a mammalian cell. We compare and discuss the relaxation times of these types. Simulations of impact with a plate are performed, and we treat the arising intracellular stresses and intercellular stresses (transmitted forces) in more detail. Finally, we show that this model is able to capture the failure dynamics of a cell.

II. METHODOLOGY

A. Cell fluid model

Parenchyma cells are typically thin walled cells that retain their content. By removing the stiff cell wall, on obtains a *protoplast* which is a soft heterogeneous substance containing water, membranes, a nucleus, organelles, macromolecules, ions, and a cytoskeleton. The latter causes that the protoplasm [30] (the living content of the cell) usually behaves like a gel-like liquid. However, in parenchyma large vacuoles are present which serve as containers for the storage of water (up to 80–90 % of the cell's volume [4]) and in addition, these cells do not have the dense cytoskeleton like in animal cells. Therefore, we will preliminary assume that the protoplasm is a Newtonian homogeneous liquid which can be described by the Navier-Stokes (NS) equations.

In SPH, the particle approximation of a function evaluation $f(\mathbf{x}_i)$ using a set of neighboring particles j can be written as

$$f(\mathbf{x}_i) \approx \sum_j \mathcal{V}_j f(\mathbf{x}_j) W_{ij}, \tag{1}$$

where $\mathbf{x}_i$ is the position of the particle, and $\mathcal{V}_i$ is the volume occupied by one particle. The approximation function is a kernel $W_{ij} \equiv W(q,s)$ were $q = r_{ij}/s$, r_{ij} is the distance from a particle i to another fluid particle j, and s is the smoothing length, representing the domain over which the particle i has interaction with particles j. It is symmetrical, i.e.,

$$W_{ij} = W_{ji}, \tag{2}$$

and should be normalized,

$$\int_{\mathcal{V}} W d\mathcal{V} = 1. \tag{3}$$

In this paper, we choose the cubic spline function $W(q,s)$ as a kernel function, which reads

$$W(q,s) = \frac{2}{3\pi s^3} \begin{cases} \frac{2}{3} - q^2 + \frac{1}{2}q^3 & 0 < q < 1 \\ \frac{1}{6}(2-q)^3 & 1 < q < 2 \\ 0 & q > 2. \end{cases} \tag{4}$$

In NS, the force $\mathbf{F}_i$ on a particle can be decomposed in a pressure driven and a viscous component. Correspondingly, a fluid particle i is moving according to a standard SPH approximation of NS for a set of surrounding particles j

$$\mathbf{F}_i = -m_i \sum_j m_j \left(\frac{P_i}{\rho_i^2} + \frac{P_j}{\rho_j^2} \right) \nabla_i W_{ij} + m_i \sum_j m_j \left(\frac{\mu_i + \mu_j}{\rho_i \rho_j} \right) \mathbf{v}_{ij} \frac{1}{r_{ij}} \frac{\partial W_{ij}}{\partial r_{ij}}, \tag{5}$$

where P is the pressure of the fluid particle, m is its mass, ρ is the density, μ is the dynamic viscosity and furthermore $\mathbf{v}_{ij} = \mathbf{v}_i - \mathbf{v}_j$ denotes the relative particle velocity. Kernels of higher order and kernel corrections may be used to improve the accuracy or stability of the method [31,32].

In the weakly compressible SPH method, it is convenient to use the following equation of state (EOS) [33] to maintain a relation between the pressure and the density,

$$P = P_0 + \kappa \left[\left(\frac{\rho}{\rho_0} \right)^7 - 1 \right], \tag{6}$$

where P_0 is the initial net pressure (turgor) across the cell, ρ_0 is the initial density of the fluid, and $\kappa = \frac{\rho_0 c^2}{7}$ is the compression modulus where c is the speed of sound of the medium. Through Eq. (6), variations in density will be penalized by increasing the pressure, thus make the fluid weakly compressible. To update the density, we use the SPH approximation of the continuity equation

$$\frac{d\rho_i^*}{dt} = \sum_j m_j \mathbf{v}_{ij} \cdot \nabla_i W_{ij} = m_i \sum_j \mathbf{v}_{ij} \cdot \nabla_i W_{ij}, \tag{7}$$

where ρ_i^* represents the density assuming a constant particle mass. The general definition of density reads of course

$$\rho_i = \frac{m_i}{\mathcal{V}_i}. \tag{8}$$

The time derivative of Eq. (8) yields

$$\frac{d\rho_i}{dt} = m_i \frac{d}{dt}\left(\frac{1}{\mathcal{V}_i}\right) + \frac{1}{\mathcal{V}_i}\frac{dm_i}{dt} = \frac{d\rho_i^*}{dt} + \frac{\rho_i}{m_i}\frac{dm_i}{dt}. \tag{9}$$

Equation (9) can be interpreted as follows. The first term is the change in density due to the deformation of the cell volume, given by Eq. (7), while the second term in Eq. (9) can be attributed to a change in water content of the cell. Since plant cells have semipermeable walls, a net transport of water through the cell wall will be established as long as the turgor pressure in the cell does not equal the osmotic potential $\Pi(\Pi<0)$ of the cell content. If the cell fluid mass loss or gain is not too high, Π can be assumed constant. This fluid mass transport through the cell wall can be computed for each particle by the following constitutive relation [4]:

$$\frac{dm_i}{dt} = -\frac{A_c L_p \rho_i}{N_f}(P_i + \Pi), \tag{10}$$

where L_p is the hydraulic conductivity which is assumed to be isotropic over the cell's surface, N_f is the number of fluid particles, and A_c is the total cell surface. If the cell absorbs water, the density will initially increase according to the last term in Eq. (9), and hence augment the pressure by Eq. (6). This is counterbalanced by the fact that the fluid will push the cell wall outward, thus, lowering the density. The final density, which should differ only slightly from the initial density, will be obtained when the fluid particles cease to move further, i.e., when there is a force balance between the fluid pressure and the cell wall stress.

B. Cell wall model

A plant cell wall is a polymerlike structure which principally cannot be described by simple linear elasticity theory. Mechanically, the cell wall material exhibits elastic and plastic behavior and energy dissipation can be attributed to viscous and structural damping. This behavior further strongly depends on the time scale [34]. On short time scales however, in which the material composition can be assumed constant, the cell wall can be seen as a thin shell structure, described by a hyperelastic or elastoviscoplastic constitutive law. In this paper, we employ a DEM procedure in which particles are distributed on a surface, having a local connectivity and interacting through discrete forces. We implement the simplest model to describe a polymer: the isotropic incompressible Neo-Hookean solid. Our ansatz is a spherical shell whereby the particles are positioned on the vertices obtained by triangulating its surface using icosahedral symmetry. These form a net of nodes with sixfold connectivity (bonds) and contain 12 so-called topological defects with a fivefold connectivity. All the particles have discrete elastic interaction forces $\mathbf{f}^e$ and a linear damping force $\mathbf{f}^v$ to account for the viscous effects. Particles which are not bonded (no fixed connectivity) are subjected to excluded volume interactions $\mathbf{f}^r$ to avoid interpenetration with other wall particles and fluid particles [see Fig. 1(a)]. The force law proposed for these interactions is similar to a Lennard-Jones (LJ) potential. The force on a cell wall particle i due to other cell wall particles (j,k) can be written as

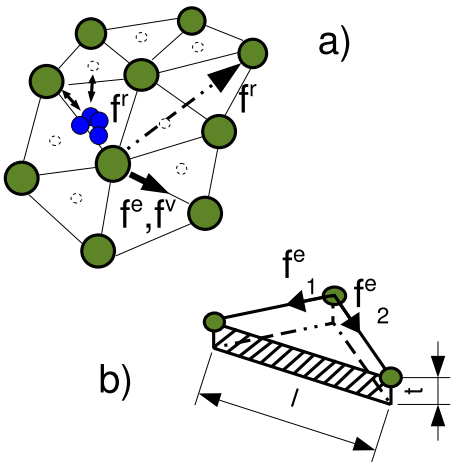

FIG. 1. (Color online) (a) Particles and their interactions involved in the model. The green particles connected with lines represent the cell wall, while the blue clustered ones represent the cell fluid. The dashed circles indicate virtual particles. Forces acting between particles are either elastic ($\mathbf{f}^e$), viscous ($\mathbf{f}^v$) or repulsive ($\mathbf{f}^r$). (b) Close up: elastic forces $\mathbf{f}^e$ acting on an opposite tether with length l and thickness t in a triangular element.

$$\mathbf{f}_i = \mathbf{f}^e + \mathbf{f}^v + \mathbf{f}^r = \sum_j \mathbf{f}^e_{ij} - \sum_j \gamma \mathbf{v}_{ij} + \sum_k f_k \mathbf{r}_{ik} + \sum_k f'_k \mathbf{v}_{ik}, \tag{11}$$

with

$$f_k = f_0\left[\left(\frac{r_0}{r_{ik}}\right)^8 - \left(\frac{r_0}{r_{ik}}\right)^4\right]\frac{1}{r_{ik}^2}. \tag{12}$$

The summation in Eq. (11) is taken over all bonded (j) and all nonbonded (k) particles. Here f_0 is the strength of the Lennard-Jones contact, and r_0 is the distance at which the force changes sign. The damping term f'_k, which depends on the stiffness of the LJ contact and the masses of the particles, is primarily meant as a noise reduction term which damps out the currently uninteresting fast behavior of the repulsive contacts. To avoid a large amount of weak interactions in the LJ term, the number of non-neighbors is limited to a cutoff distance d_{cutoff} where f_k becomes negligible. To employ the constitutive model into a discrete particle system, we first consider the stress-strain relationship for a Neo-Hookean material in principal directions i,

$$\sigma_i = G\lambda_i^2 - \sigma_0, \tag{13}$$

where G is the shear modulus of the material, λ_i is the extension ratio (in principal directions) and σ_0 is a hydrostatic constant. In case the material has the geometry of a thin spherical shell with initial radius r_0 and thickness t_0, we can consider the stretch ratios $\lambda = r/r_0$ and $\lambda_t = t/t_0$. Assuming the wall material is incompressible $(\lambda^2\lambda_t = 1)$, one has thus

$$\lambda_t = \lambda^{-2}. \tag{14}$$

Because there is little stress in the direction of the wall thickness $(\sigma_t \approx 0)$, one can calculate σ_0 and obtain the stress in the

direction of the surface meridians on the sphere under isotropic expansion

$$\sigma = G(\lambda^2 - \lambda^{-4}). \tag{15}$$

The stresses that develop in this expansion mode are used to estimate the forces between the tethers. Therefore, we start from one single triangle on the sphere. If the sphere's radius is increased or decreased, the equilateral tethers with thickness t and length l which form this triangle will change accordingly ($\lambda_l = \lambda$). The stress in the triangle can be written as the total force on a tether divided by its lateral surface area [see Fig. 1(b)].

$$\sigma_l = \frac{\|\mathbf{f}_1^e + \mathbf{f}_2^e\|}{lt}. \tag{16}$$

Owing to the triangular geometry, one obtains the elastic force between two bonds

$$f^e = \frac{Gtl}{\sqrt{3}}(\lambda_l^2 - \lambda_l^{-4}). \tag{17}$$

Furthermore, because of isotropic stretching and the incompressibility of the material

$$lt = \frac{l_0 t_0}{\lambda_l}, \tag{18}$$

one can thus conclude that the force between two particles reads

$$\mathbf{f}^e = \frac{Gl_0 t_0}{\sqrt{3}}(\lambda_l - \lambda_l^{-5})\mathbf{n}, \tag{19}$$

where $\mathbf{n}$ denotes the unit interconnecting particle vector. Note that this force model in the limit of small deformations can be regarded as a linear spring model with stiffness k where

$$k = \frac{6Gt_0}{\sqrt{3}}. \tag{20}$$

For an estimation of stress prediction errors that arise in the DEM implementation, see Appendix, Sec. 1.

Finally, the scaling of the linear damping parameter γ in Eq. (11) with macroscopic viscosity η can be done using $\eta \sim \frac{\gamma}{t_0}$, where η can be estimated from a characteristic relaxation time $\tau = \eta / E$ of the material.

C. Boundary conditions

In fluid mechanics, the contact between the fluid and the boundary is often modeled by no-slip boundary conditions. In SPH, this is accomplished by a direct fluid-boundary coupling, assuming ghost particles on the other side of the boundary [31], or simply assuming that outer SPH particles represent the boundary and superimpose elastic interactions [35]. Both approaches however are not preferable here because the first one can only treat fixed boundaries, while in the second, the boundaries do not have a distinct physical identity. In our implementation, the boundaries are represented by the discrete wall particles which repel the fluid particles by a LJ type force [see Eq. (12)], ensuring that only the normal components of the velocities of the fluid particle vanish at the boundaries. On the other hand, the soft attractive side in Eq. (12) could quantify the forces that the fluid particles need to separate from the cell wall, but this option was not elaborated further. In order to have no-slip conditions, one can include the boundary particles in the viscous part of the momentum SPH equations, but here we simply ensure this by coarsening the potential energy landscape around the boundary. By using approximately the same resolution for the SPH and DEM particles, the LJ interaction energy landscape formed by particles becomes then saddle shaped. When a fluid particle approaches boundary particles, it will be trapped in one of these potential energy wells (on the condition that its velocity is not too high), see Fig. 2. This boundary model has been tested for a 2D shear cavity test at low-Reynolds numbers [32], showing good agreement with a finite difference solution.

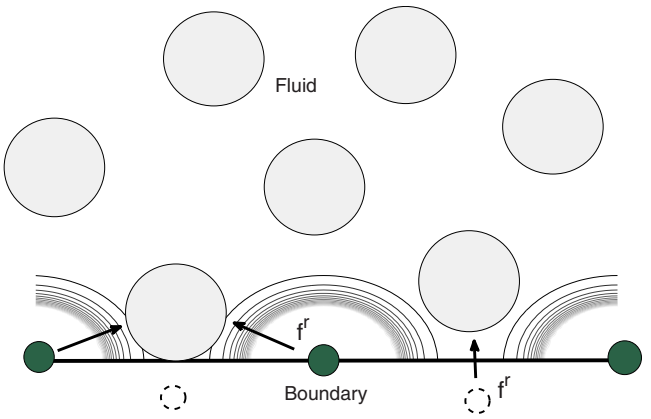

FIG. 2. (Color online) Repulsive SPH-DEM contacts: SPH particles (big circles) having contact with particles from the cell wall (small circles, equipotentials are solid lines). To prevent that SPH particles penetrate the wall, virtual particles can be added (small dashed circles) between the real particles. In this two-dimensional equivalent, the additional contact force is distributed half to both real neighboring boundary particles.

By lowering the ratio of the interparticle spacing to the LJ cutoff distance, the surface can be made smoother (slip conditions). Increasing this parameter will approximate no-slip conditions. Note that in practice, the LJ cutoff cannot be made too small compared to the interparticle distance, otherwise the fluid particles will be able to penetrate the wall. On the other hand, a too large cutoff distance results in too much distance between the fluid and the boundary particles. To prevent the fluid particles from penetrating the cell wall, without a significant increase in computational effort, "virtual" particles can be introduced. These massless particles lie in the bary center of the triangle (ijk) formed by the real particles, but can interact with the fluid particles [see Figs. 1(a) and 2]. The forces are distributed to the surrounding real particles, so that linear and angular momenta are conserved.

D. Cell initialization

Typical plant cell dimensions range from a few μm to a few hundred μm. Because of these small dimensions and the

TABLE I. Model parameters used in the cell model.

Parameter	Value (stiff cell/soft cell)	Reference
Cell wall thickness, t	126/5 nm	[36]/[37]
Cell wall Young modulus, E	2400/20 MPa	[36]/[37]
Cell radius, R	30 μm	[36]
Cell wall damping, γ	10^{-10} Nm^{-1} s	Set
Cell fluid viscosity, μ	10^{-3} Pa s−1 Pa s	Set
Fluid compression modulus, κ	10 MPa	Set
Cell turgor pressure, P_0	364/0.1 kPa	[36]/set
Cell hydraulic conductivity, L_p	10^{-12} m^2 N^{-1} s	[4,36]
SPH smoothing length, s	3.2 μm	Set
Number fluid particles per cell, N_f	3500	Set
Number wall particles per cell	2562	Set
Cell-plate contact stiffness, k_p	1000 Nm^{-1}	Set

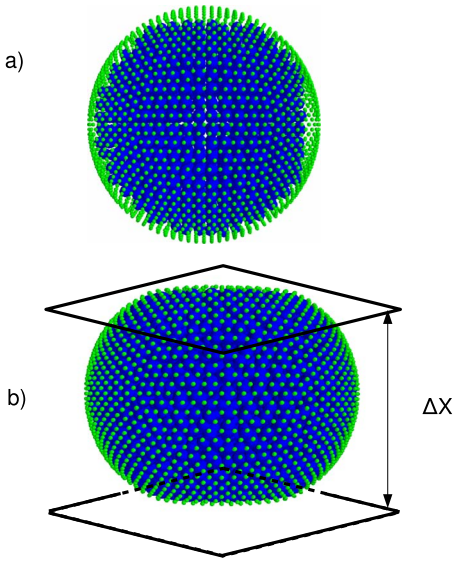

FIG. 3. (Color online) Snapshot of (a) an uninflated cell and (b) an inflated cell under compression ΔX between two plates. The big inner particles represent the cell protoplasm, the small outer particles the cell wall.

fact that biological materials generally show great variability, it is a formidable task to probe mechanical properties of cells. Moreover, plant cell walls usually have a large elastic modulus, making it difficult to measure them by AFM or optical tweezers such as is done on animal cells. Nevertheless, Wang *et al.* [36] derived a cell wall Young modulus by conducting plate compression experiments on *in vitro* tomato cells. In their model, based on the analytical calculations by Lardner and Puljara [9], the cell wall is described by a generalized Hooke's law using a Young modulus E, the initial thickness of the cell wall, Poisson's ratio ν, and the initial stretch ratio λ as physical parameters, and their model is extended with a cell wall permeability to account for volume loss during compression. The initial turgor pressure was measured. By monitoring the contact force between the cell and the plates and using model parameter fitting, the authors generally found good agreement with the experiment up to 20% of compression strain by adopting in their model a cell wall thickness 126 nm, a wall Young modulus of 2.4 GPa, and an initial wall stretch ratio of 1.015. Following the work of Wang and his co-workers, our model considers a spherical cell with radius 30 μm. The wall shear modulus is estimated by $G=E/3$ and hence we use $G=0.8$ GPa and $t_0=126$ nm in Eq. (19). In this work, we also consider another cell type, which is mechanically softer and has a lower internal pressure. This "soft" type mimics an animal cell to the degree that its wall mechanical properties are in the range of a lipid bilayer. However, it still has the same radius and the Newtonian protoplasm as in the stiff plant cell type. In fact, this cell may also be regarded as a protoplast of the plant cell. See Table I for all the input parameters.

The cell was initialized with 2562 wall particles (obtained by icosahedral triangulation, with all bond lengths l_0 approximately 2.5 μm) and 3500 fluid particles, initially positioned on a cubic lattice, but delimited by the cell's radius [see Fig. 3(a)]. For the simplicity, all LJ forces were assumed to be repulsive only [$d_{cutoff}=r_0$ in Eq. (12)]. We initially set the wall damping to an arbitrarily small value (pure elastic behavior) while still retaining stable computations. Both SPH and DEM equations of motion are integrated by a Leap-frog algorithm. The time step for the SPH equations is derived from the CFL criterion, the magnitude of particle accelerations, and viscous forces [31,32]. However, this must be combined with an additional requirement on the time step imposed by the stiffness [Eq. (20)] of the wall. In fluid dynamics, when using an EOS, the compression modulus κ plays a crucial role and should be chosen with care. If κ is large, the simulations normally will require a small time step in order to be stable. If it is chosen too low, the fluid will behave more like a compressible one. In many SPH simulations, the Mach number defines the condition to where the fluid can be regarded as incompressible [33]. Here, this condition is further restricted by the flexible boundaries. To ensure apparent incompressibility of the fluid, it is necessary to set the compression modulus sufficiently high with respect to the stiffness of the cell wall.

The cell is first simulated to grow artificially fast into a fully turgid one by setting a high hydraulic conductivity in Eq. (10). Once the fluid pressure reaches the osmotic potential [38], the cell is in mechanical equilibrium. During the inflation, the SPH particles are driven outward by the pressure, and repelled if they come too close to the cell wall. By Newton's third law, this repulsive force will in turn push the cell wall outward. As a consequence, stresses in the cell wall proportional to the fluid pressure will develop (Young-Laplace law), and the bonds between the boundary particles become slightly extended. On average, we find an initial stretch ratio of the tethers of 1.01, close to what is found by Wang and his co-workers. The SPH-DEM coupling has been benchmarked with the Young-Laplace condition, and with analytical solutions for centrosymmetric oscillations, see Appendix, Sec. 2. In Appendix, Sec. 3 we give an idea of the variations on the results that can be expected due to the discretization.

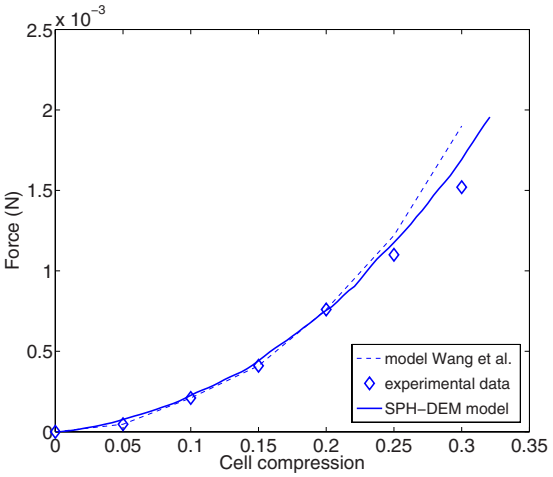

FIG. 4. (Color online) Force-displacement plot obtained by compression experiments done on an *in vitro* tomato cell, by simulations with an analytical model, and by the SPH-DEM model.

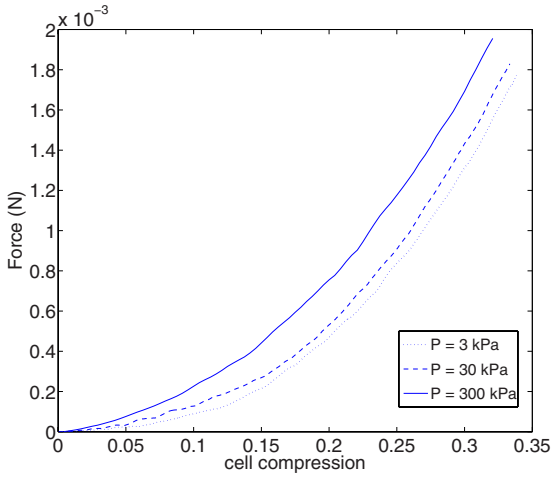

FIG. 5. (Color online) Simulated force-displacement curves obtained by compression experiments showing the effect of different turgor pressures.

III. RESULTS AND DISCUSSION

A. Quasistatic compression

Following the *in vitro* experiment conducted in [36], the stiff cell is simulated to be compressed between two flat plates. This is achieved by introducing two virtual horizontal planes with one kept at its position while the other one is moved downward by a distance ΔX [see Fig. 3(b)]. If the wall particles geometrically overlap this boundary by δ, they are repelled by a force $f_i = -k_p \delta_i$. The displacement rate was 0.002 ms^{-1}, sufficiently low to exclude inertial effects. The total force acting on the plate by the particles i is obtained by

$$F_{plate} = \sum_i - k_p \delta_i, \tag{21}$$

where k_p is chosen sufficiently large to have small δ compared to ΔX. Meanwhile, the fractional deformation of the cell $\epsilon = \Delta X / 2R$ is monitored. A resulting force/deformation plot can thus be obtained. In Fig. 4, we compare the result of this computer experiment with the experiments and analytical model provided in [36], showing good agreement for strains below 20%. For higher strains, deviations start to develop between both models and the experiment, a fact that is most likely due the yielding of the cell wall material. The differences between our model and the analytical one are due to the geometry distortion and the weak fluid compressibility. An additional simulation, performed with half of the number of the initially used SPH and DEM particles gave significantly less accurate results (not shown). This means that in order to get reliable results, the smoothing length of the SPH particles and the bond length of the DEM particles should be sufficiently small compared to the cell's dimensions.

As in [36], we did not find any effect of the hydraulic permeability: water losses are simply too low on the time scales <1 *s*. The effect of turgor, which can be highly variable during the lifetime of a cell, is addressed as well. It is shown both experimentally and by simulations that a lower turgor decreases the stiffness of the tissue. To model the effect of turgor pressure on a single cell during an external stress, we have run compression simulations with different values of initial turgor. In Fig. 5, the results from a compression simulation with initial turgor values of $P = 3$ kPa, $P = 30$ kPa, and $P = 300$ kPa are shown. From the slopes of the curves, we conclude that higher turgor indeed leads to a stiffer system, but only for small deformations (the slopes for the curves with low turgor pressure are almost zero at the beginning, contrary to those for higher turgor). At higher strain however, all curves become somewhat parallel, i.e., they exhibit the same stiffness. Similar effects are observed in experiments on fruit tissues [39].

B. Relaxation

A relaxation experiment reveals the cell's dynamic response. We simulate the viscoelastic response of a cell by releasing it from a compressed state, i.e., by suddenly removing the horizontal plates. Since the hydraulic conductivity can be discarded in this process, we only have two parameters contributing to the viscous effect: the cell wall damping parameter and the protoplasm viscosity. One could put forward that the cell content cannot be regarded as a homogeneous material and its viscous properties may vary locally. Although in the SPH formulation this could be accounted for by assigning a different viscosity to each particle, the viscous properties of the cell content are averaged here and assumed to behave Newtonian. The viscosity of pure water may therefore serve as an initial guess and lower limit, although in reality plant cells generally exhibit a larger protoplasm viscosity due to the presence of larger molecules such as polysaccharides and proteins [40,41]. The cell wall damping could in principle be related to rheological experiments, but to our best knowledge no relevant data are available on that. Stress relaxation in cell walls has been studied by rheological experiments, yet on time scales and extension ratios far beyond those in the frame we are considering. To estimate the damping parameter, one can define the parameter ζ for two connected cell wall particles

$$\zeta = \frac{\gamma}{\sqrt{2km}}, \tag{22}$$

where $k = \frac{6Gt_0}{\sqrt{3}}$ is the stiffness and m is the cell wall particle mass. The absence of viscous effects is approached if $\zeta \ll 1$, while the wall material reacts as an overdamped system if $\zeta > 1$.

To monitor the relaxation, we compute the equatorial force F_{eq} for a hemisphere,

$$F_{eq} = \sum_i \sum_j \mathbf{f}_{ij}, \tag{23}$$

where $\mathbf{f}_{ij}$ is the internal force acting on a particle i from the neighboring particles j, and the summation is over all the particles that lie on this hemisphere (see Appendix, Sec. 2, Fig. 15). In Fig. 6(a), this force is plotted as a function of time for the stiff cell type with a protoplasm viscosity range (1 mPa s–1 Pa s), assuming a purely elastic cell wall. Additionally we also show the model results for a slightly overdamped wall material ($\zeta = 1.1$). The simulations reveal that the cell, once released, oscillates several times with a period less than 1 μs and thus may be regarded as a viscoelastic solid. The oscillations are damped by both the cell fluid viscosity and cell wall damping and the fluid viscosity seems to have the major influence on this. Interestingly, the stiff cell behaves as an overdamped system if the cell fluid viscosity exceeds approximately 0.5 Pa s. Note that the response is fast and different from that of animal cells, which behave more fluidlike. For the soft cell, the equatorial forces in the relaxation experiments are depicted in Fig. 6(b), showing that this cell reacts much slower than the stiff type, and exhibits weaker oscillations. The relaxation times are 30 μs for the lowest fluid viscosity, and 5 ms for the highest (the cell wall was assumed to be elastic). We note that these relaxation times are still below these observed in animal cells, which are typically around 1 s [17,42]. The cause for this discrepancy is most likely due to the nature of the protoplasm of these cells, which is a complex fluid and where, in contrast to the plant cell type, a dense cytoskeleton plays a dominant role [37,42].

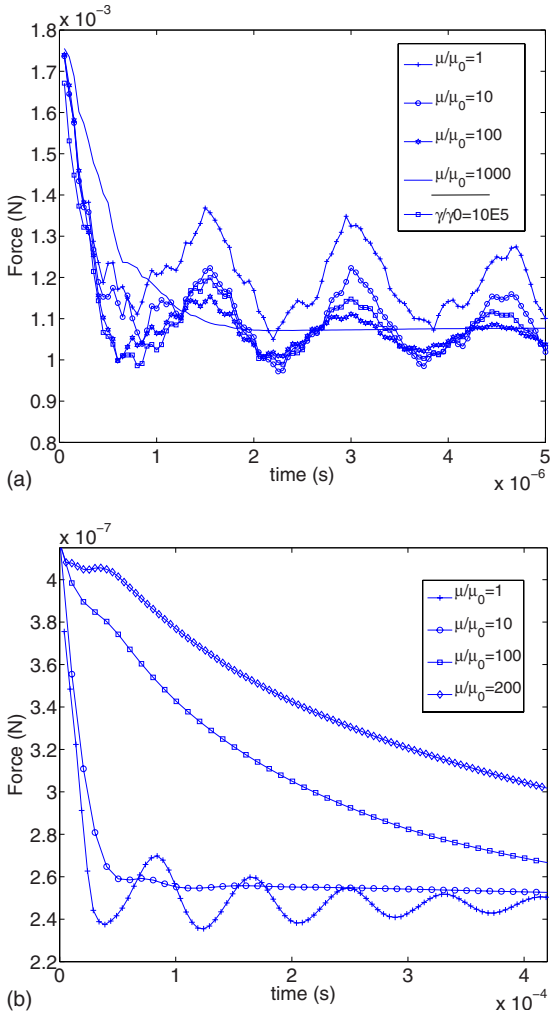

FIG. 6. (Color online) Relaxation experiment, showing the evolution of the equatorial force when releasing the cell from a compressed state, simulated for a protoplasm viscosity range of 1 mPa s–1 Pa s. μ_0 represents a viscosity of 1 mPa s. (a) Stiff cell type: the cell relaxes in about 1 μs in all cases and further oscillates except for the highest fluid viscosity (assuming a low-cell wall damping, $\zeta \ll 1$). The response for a highly damped ($\zeta = 1.1$) cell wall material is also given (γ is five orders of magnitude larger than the low damped: $\gamma_0 = 10^{-10}$ Nm s^{-1}, and $\mu = \mu_0$). (b) The soft cell relaxes in 30 μs for a low fluid viscosity. Larger values strongly increase the relaxation time. The transition to an overdamped system occurs for a fluid viscosity of approximately 10 mPa s.

C. Impact

The situation during impact is different to the one of quasistatic compression because inertia and viscous effects cannot be ignored. Impacting a cell causes additional stress components on both the cell fluid and cell wall. Here, we concentrate on the protoplasmic stresses and the forces that are transmitted by the whole cell. To this end, we start from the same simulation setup as in Sec. III A, but with a loading rate of 5 ms^{-1}. This velocity is well below the Mach number imposed by the compressibility modulus, thus ensuring the apparent incompressibility of the protoplasm during impact. We look at the two different cell types. Figure 7 provides snapshots of the two cell types at $\epsilon = 25\%$ when impacted. The shape of the cells changes as a shock wave travels through them. The resulting deformation depends on the viscosity, with a stronger effect in the soft cell, while the stiff type tends to deform more symmetrically [compare Fig. 7(a) with Fig. 7(b)]. We note the link with the relaxation experiments: the impact duration takes only about 3 μs and covers the relaxation time of the stiff cell. Contrary, it is much smaller than the relaxation time of the soft cell, and hence the latter is unable to follow the deformation.

Generally, we find that the lower the fluid viscosity, the higher the cell shape deforms during impact. This clearly visible in Fig. 7(b) for the soft cell type, which behaves more fluidlike as a whole. We visually observe that in the latter the fluid slightly and locally (in the region of the impacting object) detaches from the cell wall in case of a high protoplasm viscosity [Fig. 7(b), bottom], as it seems unable to keep up

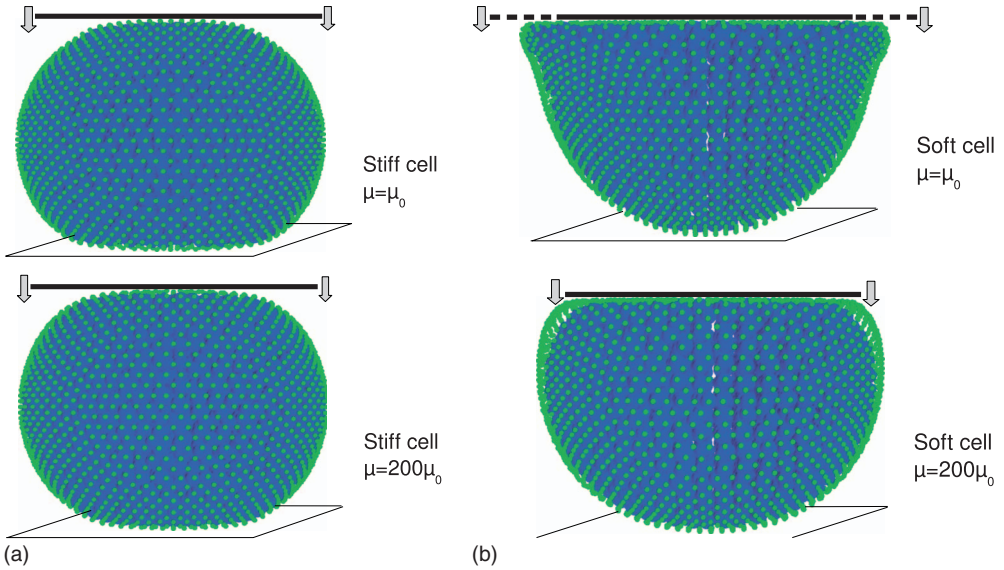

FIG. 7. (Color) Snapshots ($t=3$ μs or $\epsilon=25\%$) of a simulated cell impacted with a plate with velocity of 5 ms^{-1}, considering (a) a stiff sphere ($\mu=\mu_0$ and $\mu=200\mu_0$), (b) a soft sphere with $\mu=\mu_0$ and $\mu=200\mu_0$). Note the difference in shape of the deformed cells. During impact with the soft sphere with high viscosity the fluid slightly and locally detaches from the cell wall [see case (b), bottom figure]. μ_0 represents a viscosity of 1 mPa s.

with the motion of the cell wall. This behavior is related to the slow reaction time of the cell and was not observed in the quasistatic situation, nor in any simulations with stiff cells. Whether this behavior is physically relevant or whether it should be avoided by introducing attractive fluid-wall forces and explicitly model the gaseous pressure forces on the cell wall is an interesting question for future research [43].

Let us consider the stresses that develop inside the cell. The protoplasmic stress is defined as the fluid shear stress, i.e., the dynamic pressure components arising from the shock waves are discarded. In fluid dynamics, the viscous shear stress $\tau^{\alpha\beta}$ $(\alpha,\beta\in\{x,y,z\})$ components can be written as

$$\tau^{\alpha\beta}=\mu\left(\frac{\partial \mathbf{v}^{\beta}}{\partial \mathbf{x}^{\alpha}}+\frac{\partial \mathbf{v}^{\alpha}}{\partial \mathbf{x}^{\beta}}\right), \tag{24}$$

where $\mathbf{v}$ is the fluid velocity field. The corresponding SPH discretization for each particle reads

$$\tau_i^{\alpha\beta}\sim\mu_i\left(\sum_j \frac{m_j}{\rho_j}\mathbf{v}_{ji}^{\beta}\frac{\partial W_{ij}}{\partial \mathbf{x}_i^{\alpha}}+\sum_j \frac{m_j}{\rho_j}\mathbf{v}_{ji}^{\alpha}\frac{\partial W_{ij}}{\partial \mathbf{x}_i^{\beta}}\right). \tag{25}$$

We further define the total effective shear stress τ in a particle as

$$\tau_i=\sqrt{(\tau_i^{xy})^2+(\tau_i^{xz})^2+(\tau_i^{yz})^2}. \tag{26}$$

Simulations were run capturing the situation at the onset of compression ($\epsilon=4\%$) where the static turgor pressure is relatively constant. A topographic mapping (Fig. 8) provides a view on the particle stress distribution, and indicates that a zone with significant stresses covers roughly one fifth of the cell area below the impact zone. The magnitude of the developed stresses depends on the protoplasm viscosity and the impact velocity. For the stiff cell type, linear behavior is observed in the low viscosity cases with an average stress in the impact region of 250 and 2450 Pa for a protoplasm viscosity of 1 and 10 mPa s, respectively. For the high-viscosity (1 Pa s) the average stress is about 180 kPa, thus locally exceeding the initial hydrostatic pressure. For this viscosity, the stresses are below the linear expectation, meaning that the particle shear relative velocities have decreased. For the soft types, the results are in the same range, meaning that the stresses are largely exceeding the initial hydrostatic pressure for the highest viscosity. Additional simulations capturing the situation at a higher compression ($\epsilon=10\%$) do not result in remarkably larger values of the shear stresses, which indicates that significant protoplasmic stresses develop even at a very low compression strains.

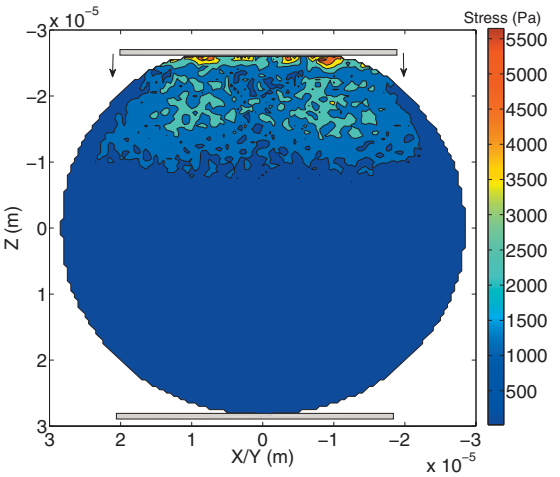

FIG. 8. (Color) Simulated protoplasmic effective shear stresses that develop at impact, as a function of the projected position in the $(X\text{-}Y,Z)$ plane of the cell for a fluid viscosity of 10 mPa s at an impact speed of 5 ms^{-1} (4% of compression).

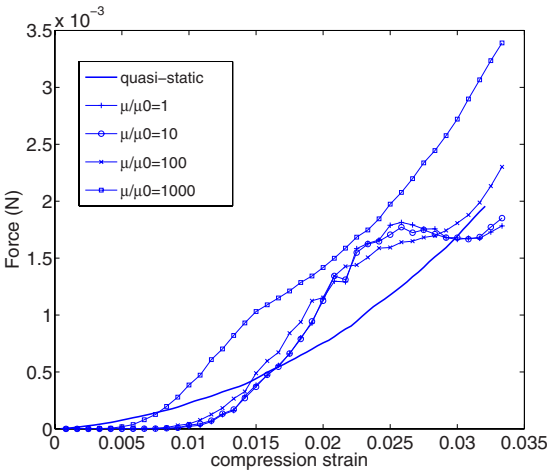

FIG. 9. (Color online) Transmitted force by the stiff cell at impact (5 ms^{-1}) as a function of the compression strain on the opposite cell side for different protoplasm viscosities. The quasistatic force is also depicted. μ_0 represents a viscosity of 1 mPa s.

The transmitted force [Eq. (21)] is defined as the force that is measured on one side of a cell with an impact region on the opposite side. Figures 9 and 10 show the transmitted forces as a function of compression strain on the opposite cell side for different cell protoplasm viscosities. With both cell types, it can be clearly seen that an impact situation is quite different from the quasistatic case. Because of the inertia, a lag phase exists between this perturbation and the transmitted force. However, once this phase is past the forces build up quickly and exceed those in the quasistatic case. For the stiff cell, this effect remains quite modest for a viscosity up to 0.1 Pa s, but becomes strongly manifested for a viscosity of 1 Pa s, see Fig. 9. In the latter case the lag phase is shorter and hence one could state that the cell behaves more rigid [visible by comparing the top and bottom pictures in Fig. 7(a)] whereby the momentum is merely transferred downward by pressure forces and less toward the transverse

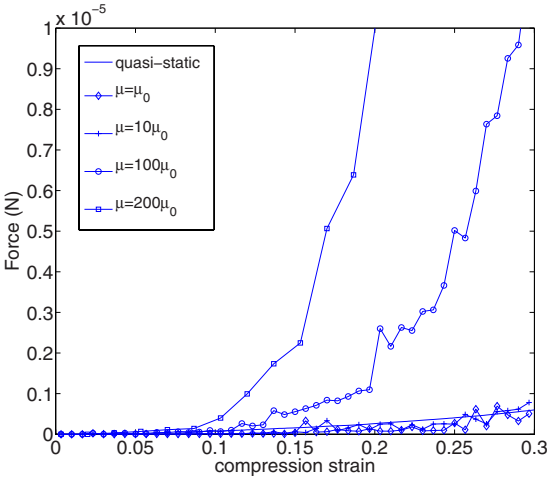

FIG. 10. (Color online) Transmitted force by the soft cell at impact (5 ms^{-1}) as a function of the compression strain on the opposite cell side for different protoplasm viscosities. The quasistatic force is also depicted. μ_0 represents a viscosity of 1 mPa s.

sides of the cell (which introduces shear). In the soft cell type, the viscous forces play a much larger role than the pressure forces, as the force transmission builds up relatively fast at a lower viscosity, see Fig. 10.

These simulations can provide estimations of how much stress the vital parts in a cell will bear on impact, a subject where little research has been conducted on so far. More accurate and local results can be obtained using a finer particle discretization, i.e., a lower smoothing length compared to the cell's dimensions. On the other hand, such a refinement should go along with capturing more detail of the cellular content, by identifying particle clusters with certain substructures in the cell. Although this approach is well suited for these kind of problems, such additional work remains out of the scope of this paper.

D. Failure of the cell

The causes for the failure of a thin fluid-filled shell can either be internal (e.g., because of an excessive pressure) or external (e.g., impact with another object). Microscopically, the failure of materials originates at local weaknesses or defects in the material from where the fracture propagates further on. The modeling of cracks and their propagation in materials is an involved task whereby one could rely on multiscaling approaches. Nevertheless, DEM models employed to simulate the breakup of shells have been able to reproduce the mass fragmental distribution in experiments after impact or explosion [44]. As in the latter, we implement a failure criterion by assuming a threshold for the local strains between two neighboring particles. Our model thus can only capture crack propagation with limited detail, but it has the advantage that fluid interaction is taken into account in a consistent way, allowing to make quantitative predictions about the behavior of a cell during and after failure. This could be of particular interest when one focuses on the cell aggregates, where the mechanics is not only determined by a single cell but also depends on interactions with neighboring cells.

We consider a stiff cell type and assume that a tether on the membrane fails when its stretch ratio exceeds a critical value λ_f. Since from a material science viewpoint a great biological variability can be expected we shall not focus on the absolute values of this critical extension. A simulation considering quasistatic compression was run with arbitrarily $\lambda_f = 1.04$. This corresponds to a cell compression strain $\epsilon_f = 14\%$, the point from where the cell starts to fail [see Fig. 11(a)]. A main fracture originates near the equator and proceeds toward the poles, where it stops (this process takes less than 0.5 μs). This can indeed be expected as the largest wall stresses will be those in the directions parallel to the equator. As a result of the crack, a jet of fluid escapes from the two partially attached halves (the particle speeds in this jet are around 3 ms^{-1}) [45]. The behavior during impact shows quite a different picture. Due to the asymmetry arising from the inertial effects, the fracture originates in the region of the impacting object where the wall is deformed the most, and occurs faster in terms of compression strain. This effect is stronger for a low fluid viscosity, where the cell wall suffers

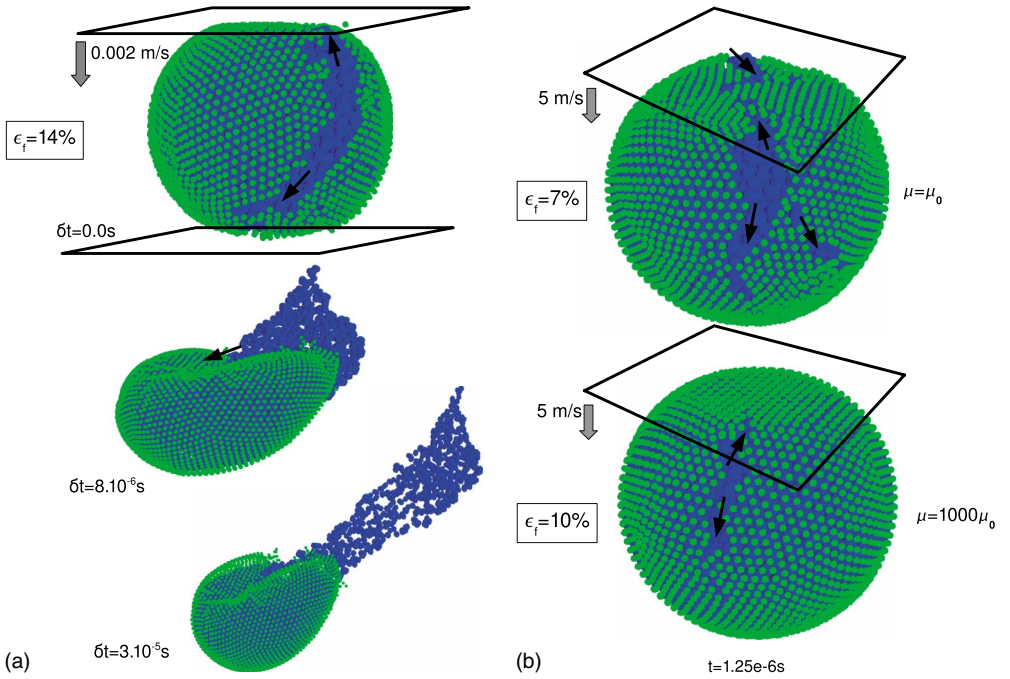

FIG. 11. (Color online) (a) Snapshots of a stiff cell bursting due to excessive load in a quasistatic compression experiment. The cell wall started ripping open near the equator of the cell ($\delta t=0$ s) and proceeds toward the poles. After $\delta t=3\times10^{-5}$ s the cell has almost completely ripped open, producing two halves from where the fluid further escapes. (b) Snapshots (both at time $t=1.25$ μs) of a cell bursting due to excessive load in a 5 ms^{-1} impact experiment. Top: for a fluid viscosity of 1 mPa s; bottom: for a fluid viscosity of 1 Pa s. All simulations are performed with $\lambda_f=1.04$. ϵ_f denotes the compression strain at which the failure occurs. The arrows indicate the crack propagation direction. μ_0 represents a viscosity of 1 mPa s.

more severe fracture, arising at $\epsilon_f=7\%$ [see Fig. 11(b), top]. For a high-fluid viscosity, a single fracture occurs at $\epsilon_f=10\%$ [see Fig. 11(b), bottom]. We note that this is in agreement with the observation mentioned in the previous section, i.e., that larger local deformations of the cell shape arise in case of lower protoplasm viscosities. Thus, although a cell with a high-protoplasm viscosity generally suffers higher intracellular stresses and yields higher transmitted forces, its cell wall may bear lower stresses leading to less fracture susceptibility during impact. Whether and how these mechanisms are related to the well-known fact that bruise volumes in fruits tend to increase with lower temperatures [7] (and thus higher viscosities) is something that should be pursued in the future.

IV. CONCLUSION AND OUTLOOK

This paper has been concerned with the modeling of the micromechanical response of a spherical biological cell. To this end, we have considered a plant parenchyma cell, which is regarded as a thin walled liquid filled capsule, and presented a model that couples a Newtonian liquid and a viscoelastic polymeric solid. This has been achieved, respectively, by the integration of SPH and a DEM into a particle framework. A standard weakly compressible SPH technique was applied to the cell protoplasm while the effects of the hydraulic permeability of the cell were built in through a constitutive relation in the SPH formulation. We assumed a Neo-Hookean behavior of the cell wall and the DEM model was constructed with particles having a sixfold connectivity. The SPH-DEM combination holds acceptable accuracy concerning static mechanical equilibrium (Young-Laplace) and the analytical solutions of centrosymmetric oscillations. In addition, good agreement was found with an analytical solution and experiments during compression of an *in vitro* plant cell. Therefore, it could be stated that the overall response of the cell to mechanical stimuli is well covered by this model.

In order to explore the micromechanics of a cell, simulations have been performed considering various situations. Under quasistatic stress conditions, we reproduce that the cell's response is highly dependent on turgor pressure, i.e., higher turgor pressure produces stiffer cells (and thus tissues), a fact that is well described in literature. More importantly however, this model is also able to capture dynamic situations. For this, we looked at the behavior of two distinct cell types, namely, a stiff cell type (plantlike), and a soft cell type (animal-like). In relaxation experiments we show that both cell responses can be compared to a viscoelastic solid, whereby both the dissipating effects in the cell wall and protoplasm play a role, though those in the latter are dominant. We have found that the response time of the stiff cell is about 1 μs as long as the viscosity of the protoplasm is below approximately 1 Pa s. For the soft cell, this is 30 μs as long as the viscosity of the protoplasm is below approximately 0.2 Pa s. A higher viscosity (up to 1 Pa s) increases the response time of the soft cell, but hardly affects the stiff cell. We have also considered an impact situation in which the cells are compressed at a rate of 5 ms^{-1}, corresponding to a transient state lasting only a few μs. Inside the cell, proto-

plasmic shear stresses develop in the impact zone, and these are linearly related to the viscosity for low-viscosity values, but become lower than linear as the viscosity increases. The simulations further show that the force transmission through the cell at impact is very different from that of a low loading rate. Due to inertial effects, the force transmitted by the cell is lagged compared to the perturbation, but then rises more quickly. Higher protoplasm viscosities decrease this lag and yield a higher transmitted force, making the overall response more rigid. Again, we notice a distinct behavior regarding the cell type. The stiff cell seems to be able to follow the perturbation, but the soft cell does not: it deforms more and is more susceptible to the protoplasm viscosity.

The strength and failure of shells enclosing a gas or liquid is an important issue in engineering and even daily life, and relates also to microscopic scales, as cells build up to tissue. By introducing a critical strain in a bond between two particles, we have shown that the dynamics of cell failure can be modeled quantitatively. Under quasistatic loading, fracture originates at the equator of the cell and propagates further toward the poles. This is in contrast with the impact loading where the fracture originates near the impact region, is affected by the protoplasm viscosity, and occurs at a relatively low compression strain.

As a conclusion, we have shown that this combination of two particle methods generates possibilities for simulating cellular mechanics. A strong advantage is the adaptivity of the method, which should make a cell centered approach possible, a task that will be harder to implement in a FEM approach [24]. Adding more particles to the system can result in two different approaches. In fine-grained models of a cell, one could capture more subcellular detail, which is essentially important for a better understanding of the relation between cellular micromechanics and biological processes. For example, particles or particle clusters can be viewed as cell organelles or the cytoskeleton [26,35]. From another viewpoint, by integrating cells to an aggregate, and introduce cell-cell adhesion, yielding, and debonding mechanisms, a resulting multicellular system can provide answers to problems related to the tissue scale [6]. Considering the benefits of SPH, one could particularly investigate the micromechanical cellular stresses in tissues that develop during short and violent situations.

ACKNOWLEDGMENTS

This research is conducted utilizing high-performance computational resources provided by the University of Leuven, http://ludit.kuleuven.be/hpc. The authors would like to thank Onderzoekstoelage (OT, KULeuven) and the Research Foundation-Flanders (FWO-Vlaanderen) for financial support. We are also grateful to Johan Meyers (KULeuven).

APPENDIX: ERROR ESTIMATIONS

1. Accuracy of the triangulated particle cell wall model during deformations

A triangulated particle discretization with equilateral tethers predicts the stress exactly under isotropic stretch, which applies to a flat surface under equibiaxial stretch. However, when such a sphere is deformed due to external forces, the assumed isotropy disappears. To quantify how the network reacts on anisotropic stresses, we consider a rectangular sheet with length L and thickness t consisting of equilateral triangles (400 nodes), see Fig. 12. We then assume two distinct loading cases of uniaxial stretching: one where the perpendicular sides are fixed, and one where they are free. As a consequence, different stresses will develop on the perpendicular sides. These two cases can be computed analytically and compared with computer experiments. In the case where only one side is fixed, the total force can be written as

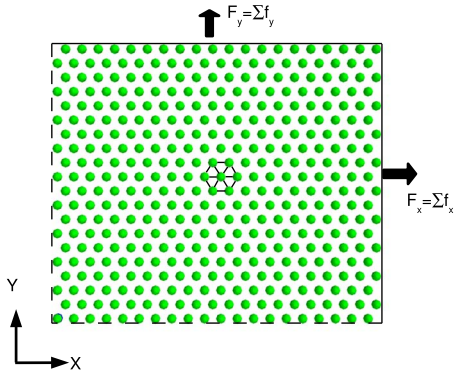

FIG. 12. (Color online) Loading modes of a rectangular sheet rendered with triangular nodes. Simulations have been carried out while measuring the boundary forces on the sheet when extending in X or Y direction. Two distinct cases were considered: one where only the opposite side is fixed, but the two other ones are free, and one where all remaining sides are locked.

$$F_{sheet} = GL_0t_0(\lambda_L^2 - \lambda_L^{-2}). \tag{A1}$$

In case there are no free ends, one has

$$F_{sheet} = GL_0t_0(\lambda_L^2 - \lambda_L^{-1})\sqrt{\lambda_L}. \tag{A2}$$

In Figs. 13 and 14, the results of these simulations are shown. Note that for each case two simulations were run: one in the direction X parallel to one of the sides of the triangle (there are three possible directions), and one perpendicular to the latter (Y). This is to show how the anisotropy manifests in the network. However, as can be observed in Fig. 13, we still have good agreement in the first case up to a stretch ratio of 1.2, and the anisotropy is still limited. In the second case (Fig. 14), the model overestimates the stress in the beginning of stretching although the deviations remain below 20%, (here the anisotropy is higher). It is thus clear that large distortions in the particle topology will yield less accurate results. However, in the main text it is shown that the DEM model can still produce accurate results in case of the quasistatic compression of a cell.

2. Numerical consistency of the DEM-SPH mechanical coupling

The cell is simulated to grow artificially fast into a fully turgid one by setting a high hydraulic conductivity in Eq. (10). Once the fluid pressure reaches the osmotic potential,

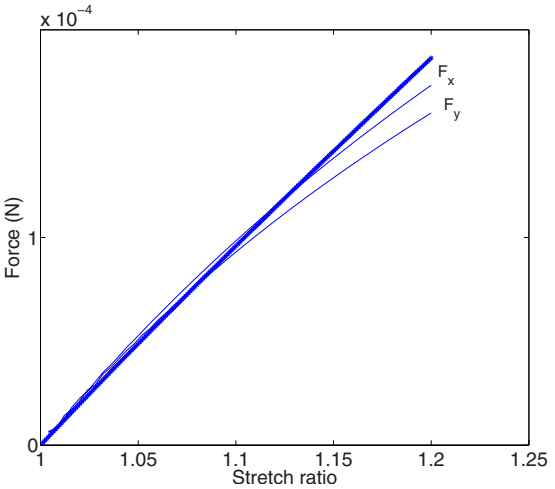

FIG. 13. (Color online) Comparison of the total theoretical force (indicated by *) obtained by Eq. (21) and the force obtained by the particle cell wall model in two perpendicular directions (X,Y), by uniaxial extension of a rectangular sheet, keeping the remaining two opposite sides fixed.

the cell is in mechanical equilibrium. During the inflation, the SPH particles are driven outward by the pressure, and repelled if they come too close to the cell wall. By Newton's third law, this repulsive force will in turn push the cell wall outward. As a consequence, stresses in the cell wall proportional to the fluid pressure will develop (Young-Laplace law), and the bonds between the boundary particles become slightly extended. On average, we find an initial stretch ratio of the tethers of 1.01, close to what is found by Wang and his co-workers. However, it is not automatically guaranteed that the Young-Laplace law is fulfilled in the SPH-DEM combination. To verify this, we consider a hemisphere with radius R, see Fig. 15. The theoretical force F on the boundary ring (with has thickness t) is then given by

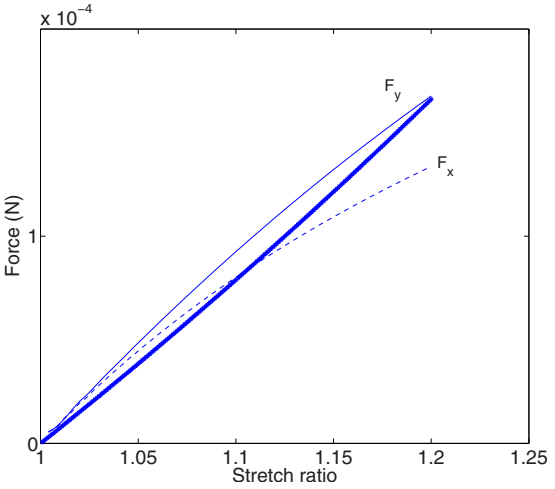

FIG. 14. (Color online) Comparison of the total theoretical force (indicated by *) obtained by Eq. (21) and the force obtained by the particle cell wall model in two perpendicular directions (X,Y), by uniaxial extension of a rectangular sheet, keeping the remaining two opposite sides free.

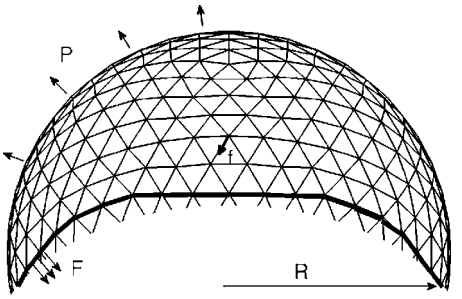

FIG. 15. Discrete forces (f) acting on the nodes of the triangulated spherical cap, resulting in a boundary force (F) when a fluid pressure P is present.

$$F = P\pi R^2. \tag{A3}$$

This force should equal F_{eq} in Eq. (23). Simulations considering a stiff cell type performed with $P=(0.1,0.2,0.4)$ MPa show an acceptable agreement with errors below 5%. This quasi-ensures that the hydrostatic coupling between the cell fluid pressure and cell wall tension is automatically guaranteed in the model.

We further validate the model by comparing it with analytical solutions concerning the small radial oscillations of a fluid-filled, thin spherical shell with radius R. The analytical equation that yields the frequencies ω of this system is well known [46],

$$\frac{j_0(q)}{j_1(q)} - \frac{q\rho_s t}{\rho R} + \frac{4Et}{q\rho c^2 R} = 0, \tag{A4}$$

where c, $\rho(=1000\ \mathrm{kg/m^3})$ are the speed of sound in the fluid and its density, and ρ_s, E are the density and the Young modulus of the wall material. Furthermore, j_k are the spherical Bessel functions of the first kind, with $q=\omega R/c$.

We now consider two cases. In a first case, the shell is completely *in vacuo*. This case is obtained by either setting $c\to 0$ (corresponding to zero momentum transfer between fluid and wall), or setting $\rho\to 0$ (no fluid mass) in Eq. (A4). The cell surface will oscillate with a ground frequency,

$$\omega = \frac{1}{R}\sqrt{\frac{4E}{\rho_s}}. \tag{A5}$$

In the model, an oscillation can be triggered easily by considering a pressurized cell and suddenly remove the enclosed fluid. By using the values from Table I with $E=3G$, and computing $\rho_s=M_{cellwall}/4\pi R^2 t$, we find $\omega=3.451\times 10^7\ \mathrm{s^{-1}}$ (stiff sphere) and $\omega=5.943\times 10^5\ \mathrm{s^{-1}}$ (soft sphere) analytically. The simulation results determining the period of the radial oscillations of the cell wall are within 1% deviation of these solutions.

Second, we consider the case that the sphere contains a compressible liquid. The analytical solution for the vibrations of this system is somewhat more complicated, as there are more possible frequencies which can be excited. In our model, we excite the system by giving the wall particles an initial inward radial velocity. The cell will then start to oscillate around its initial state. In Figs. 16(a) and 16(b) the spectrum of excited frequencies is given for $c=50\ \mathrm{ms^{-1}}$ and

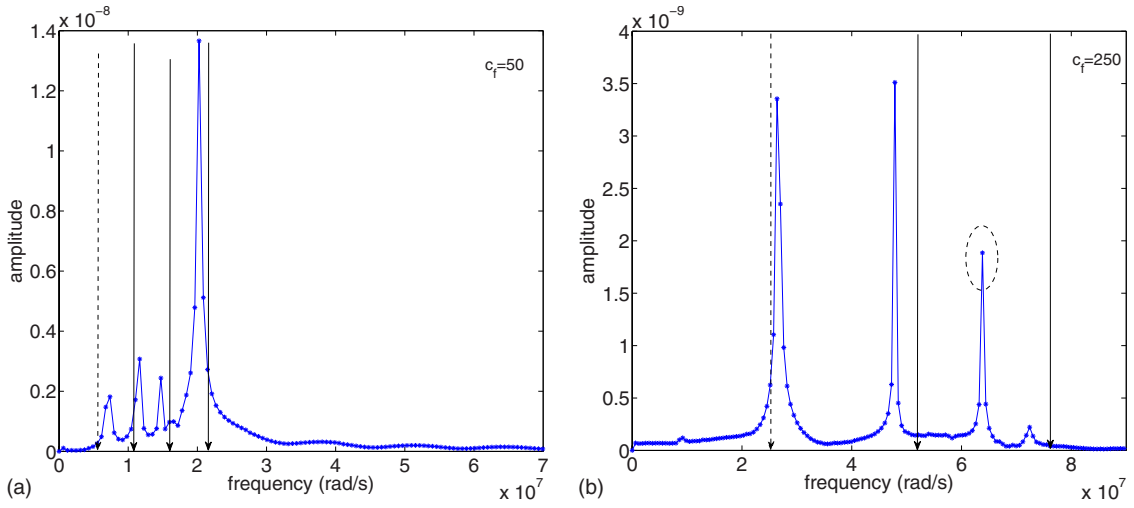

FIG. 16. (Color online) [(a) and (b)] Frequency spectra of the oscillations with $c=50$ ms^{-1} and $c=250$ ms^{-1}, respectively. The arrows indicate analytical solutions; the dashed arrow the ground frequency. Not all analytical solutions are shown.

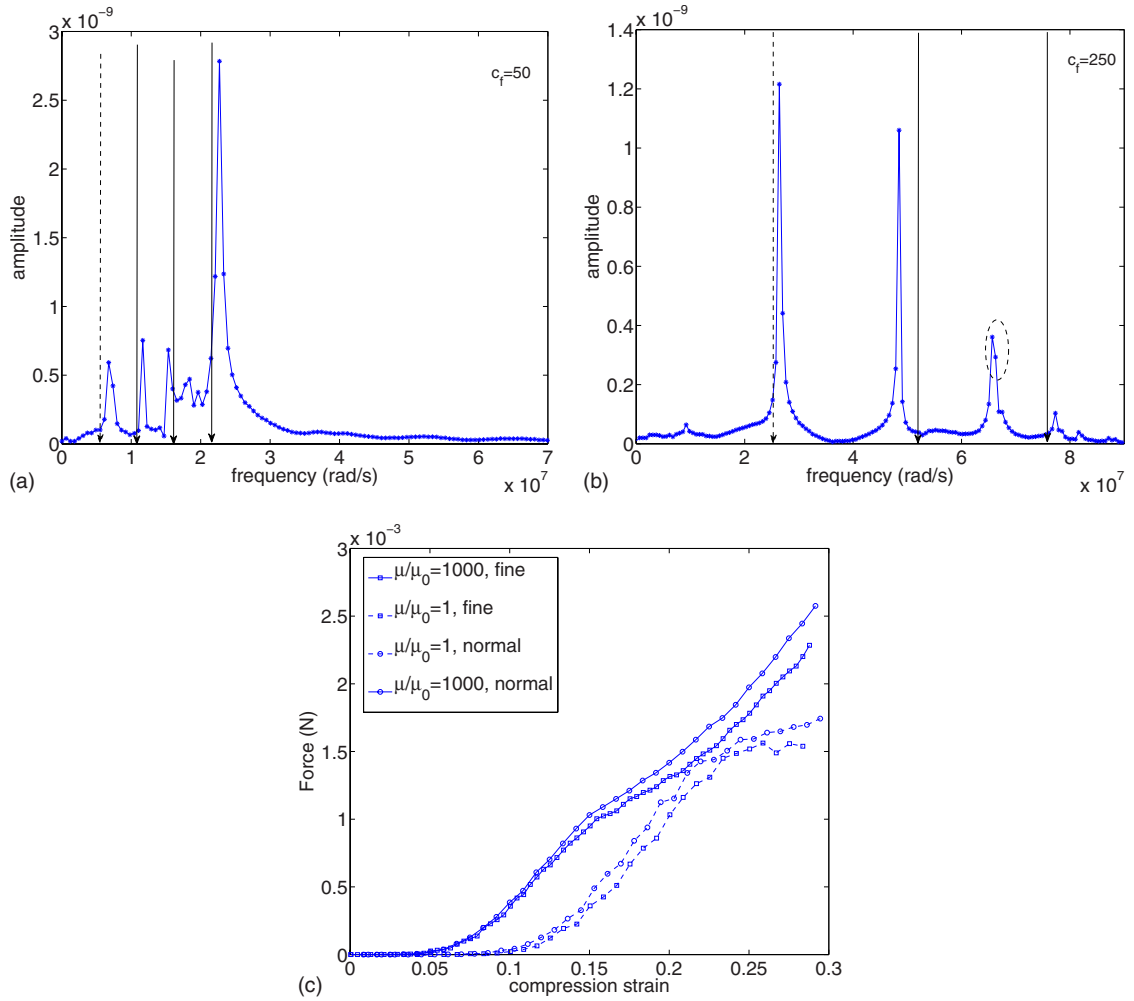

FIG. 17. (Color online) [(a) and (b)] Frequency spectra obtained from oscillations of a stiff cell with $c=50$, 250 ms^{-1} using 14 000 SPH particles and 10 242 DEM particles ("fine"). (c) Comparison of force-compression curves at impact for a stiff cell type, obtained for the initial used number of SPH-DEM particles, and with a fine discretization.

$c=250$ ms^{-1}, respectively. In addition, the theoretical frequencies are also shown (arrows). The dashed arrows indicate ground frequencies. For low c (<50 ms^{-1}), the frequencies are close to each other and a comparison with the analytical solution is difficult. For higher values of c the comparison becomes clearer. The model captures the ground mode and at least two higher frequencies reasonably (deviations are between 5% and 10%, due to the discretization errors and the fluid-boundary coupling). For the large c [Fig. 16(b)], a mode shows up which is not close to any analytical solution (indicated by dashed ellipse). We address this discrepancy between model and analytical solution to the influence of the LJ connection between boundary and fluid, which is not accounted for in Eq. (A4). However, we argue that in the case of high κ ($c=265$ ms^{-1} is used in the simulations), the influence of the latter can be minimized because the time scale of the dynamics we are considering here (e.g., impact, relaxation) is ten times higher, and in addition, the amplitudes of these oscillations are relatively small. The first two frequencies are within 6% deviation from the analytical solution.

3. Particle discretization

We have also tested the model for numerical consistency by performing simulations with four times the number of SPH-DEM particles. In Figs. 17(a) and 17(b) the frequency spectrum for the centrosymmetric oscillations in the case of $c=50$ ms^{-1} and $c=100$ ms^{-1} are depicted. The results are comparable with the coarser discretization although showing a slightly better agreement with the analytical solutions. Furthermore, it is shown in Fig. 17(c) that for the impact of the cell, the initial and the fine discretization hold an acceptable consistency.

[1] J. Dumais, Cur. Op. Plant Biol. **10**, 58 (2007).
[2] F. Guilak, J. R. Tedrow, and R. Burgkart, Biochem. Biophys. Res. Commun. **269**, 781 (2000).
[3] Y. Liu, F. Schieving, J. F. Stuefer, and N. P. R. Anten, Ann. Bot. (London) **99**, 121 (2007).
[4] L. Taiz and E. Zeiger, *Plant Physiology* (Sinauer Associates, Sunderland, MA, 2002).
[5] Y. Forterre, J. M. Skotheim, J. Dumais, and L. Mahadevan, Nature (London) **433**, 421 (2005).
[6] P. Van Liedekerke, P. Ghysels, E. Tijskens, G. Samaey, B. Smeedts, D. Roose, and H. Ramon, Phys. Biol. **7**, 026006 (2010).
[7] M. Van Zeebroeck, V. Van linden, P. Darius, B. De Ketelaere, H. Ramon, and E. Tijskens, Postharvest Biol. Technol. **46**, 10 (2007).
[8] S. B. Nilsson, C. H. Hertz, and S. Falk, Physiol. Plant. **11**, 818 (1958).
[9] T. J. Lardner and P. Pujara, Mechanics Today **5**, 161 (1980).
[10] R. E. Pitt, Trans. Am. Soc. Agric. Eng. **25**, 17761784 (1982).
[11] Q. Gao and R. E. Pitt, Trans. Am. Soc. Agric. Eng. **34**, 232 (1991).
[12] M. A. J. Chaplain, J. Theor. Biol. **163**, 77 (1993).
[13] H. I. Wu, R. D. Spence, P. J. H. Sharpe, and J. D. Goeschl, Plant, Cell Environ. **8**, 563 (1985).
[14] H. X. Zhu and J. R. Melrose, J. Theor. Biol. **221**, 89 (2003).
[15] A. E. Smith, K. E. Moxham, and A. P. J. Middelberg, Chem. Eng. Sci. **53**, 3913 (1998).
[16] J. G. McGarry and P. J. Prendergast, Eur. Cells Mater **7**, 27 (2004).
[17] S. A. Sandersius and T. J. Newman, Phys. Biol. **5**, 015002 (2008).
[18] D. M. Bruce, Philos. Trans. R. Soc. London, Ser. B **358**, 1437 (2003).
[19] J. Loodts, E. Tijskens, W. Chunfang, E. Van Streels, B. M. Nicolai, and H. Ramon, J. Texture Stud. **37**, 16 (2006).
[20] J. J. Monaghan, Annu. Rev. Astron. Astrophys. **30**, 543 (1992).
[21] M. Ellero and R. Tanner, J. Non-Newtonian Fluid Mech. **132**, 61 (2005).
[22] A. Rafiee, M. T. Manzari, and M. Hosseini, Int. J. Non-Linear Mech. **42**, 1210 (2007).
[23] Y. Zhu and P. J. Fox, Transp. Porous Media **43**, 441 (2001).
[24] S. Li and W. K. Liu, *Meshfree Particle Methods* (Springer-Verlag, Berlin, 2004).
[25] P. Español and M. Revenga, Phys. Rev. E **67**, 026705 (2003).
[26] A. Vázquez-Quesada, M. Ellero, and P. Español, J. Chem. Phys. **130**, 034901 (2009).
[27] A. Vázquez-Quesada, M. Ellero, and P. Espanol, Phys. Rev. E **79**, 056707 (2009).
[28] P. Ghysels, G. Samaey, E. Tijskens, P. Van Liedekerke, H. Ramon, and D. Roose, Phys. Biol. **6**, 016009 (2009).
[29] P. Ghysels, G. Samaey, P. Van Liedekerke, E. Tijskens, H. Ramon, and D. Roose, Int. J. Multiscale Comp. Eng. (to be published).
[30] Although the protoplasm is the content that is surrounded by a plasma membrane, we will use this term for everything except the cell wall that covers the cell's interior.
[31] J. P. Morris and P. J. Fox, J. Comput. Phys. **136**, 214 (1997).
[32] G. R. Liu and M. B. Liu, *Smoothed Particle Hydrodynamics—A Meshfree Particle Method* (World Scientific Publishing, Singapore, 2003).
[33] J. J. Monaghan, J. Comput. Phys. **110**, 399 (1994).
[34] B. A. Veytsman and D. J. Cosgrove, Biophys. J. **75**, 2240 (1998).
[35] S. M. Hosseini and J. J. Feng, Chem. Eng. Sci. **64**, 4488 (2009).
[36] C. X. Wang, L. Wang, and C. R. Thomas, Ann. Bot. (London) **93**, 443 (2004).
[37] D. Boal, *Mechanics of the Cell* (Cambridge University Press, Cambridge, 2002).
[38] In the simulations, the pressure obtained by inflation using Eq. (10) is always slightly lower (maximum 2%) than the prescribed osmotic pressure because the osmotic pressure is only reached asymptotically. Note also that in SPH an equation of state introduces noise on the pressure. Although this noise can be suppressed with kernel filters, we shall always consider the cell averaged pressure in the following.

[39] M. L. Oey, E. Vanstreels, J. De Baerdemaker, E. Tijskens, H. Ramon, M. Hertog, and B. M. Nicolai, Postharvest Biol. Technol. **44**, 240 (2007).
[40] F. Fushimi and A. Verkman, J. Cell Biol. **112**, 719 (1991).
[41] P. Scherp and K. H. Hasenstein, Am. J. Bot. **94**, 1930 (2007).
[42] F. Wottawah, S. Schinkinger, B. Lincoln, R. Ananthakrishnan, M. Romeyke, J. Guck, and J. Kas, Phys. Rev. Lett. **94**, 098103 (2005).
[43] Nevertheless, in plant cells, the protoplast can detach from the cell wall in *plasmolyzed* cells [4], which have lost a part of their water content and where the turgor pressure approaches zero.
[44] F. K. Wittel, F. Kun, H. J. Herrmann, and B. H. Kroplin, Phys. Rev. E **71**, 016108 (2005).
[45] Note that protoplasm surface tensions are discarded.
[46] P. M. Morse and H. Feshbach, *Methods of Theoretical Physics* (McGraw-Hill, New York, 1953).